nature physics

Article

https://doi.org/10.1038/s41567-025-02873-1

Skyrmion bags of light in plasmonic moiré superlattices

Received: 17 September 2024

Accepted: 10 March 2025

Published online: 22 April 2025

Check for updates

Julian Schwab[1], Alexander Neuhaus[2], Pascal Dreher[2], Shai Tsesses[3], Kobi Cohen[3], Florian Mangold[1], Anant Mantha[1], Bettina Frank[1], Guy Bartal[3], Frank-J. Meyer zu Heringdorf[2], Timothy J. Davis[1,2,4] & Harald Giessen[1]

The study of van der Waals heterostructures with an interlayer twist, known as twistronics, has been instrumental in advancing the understanding of many strongly correlated phases, many of which derive from the topology of the physical system. Here we explore the application of the twistronics paradigm in plasmonic systems with a non-trivial topology by creating a moiré skyrmion superlattice using two superimposed plasmonic skyrmion lattices with a relative twist. We measure the complex electric field distribution of the moiré skyrmion superlattice using time-resolved polarimetric photoemission electron microscopy. Our results show that each supercell has very large topological invariants and harbours a skyrmion bag, the size of which is controllable by the twist angle and centre of rotation. Our work indicates how twistronics can enable the creation of various topological features in optical fields and provides a route for locally manipulating electromagnetic field distributions.

Moiré patterns can emerge from the interference of two layers of a repeating pattern with a relative twist between them[1]. Moiré patterns were originally observed in overlays of thin fabrics called moiré, from which they derive their name, but have found diverse applications beyond textiles and artworks. In microscopy, moiré patterns enable super-resolution[2], and in photonics, they provide a mechanism for creating and manipulating the spacing of optical lattices with light[3–7] and matter[8,9]. Moiré superlattices have had a profound impact in condensed matter physics, particularly in heterostructures like twisted bilayer graphene. These superlattices are responsible for such groundbreaking findings as unconventional superconductivity[10], ferroelectricity[11] and correlated insulator states[12]. The underlying mechanism for many of these exotic phases is the topology of the condensed matter system, such as flat moiré minibands with a non-trivial topology that enables ferromagnetism and the (fractional) quantum anomalous Hall effect in Chern insulators[13,14], or charged skyrmions in bilayer graphene that facilitate superconductivity at 'magic' angles[15].

Skyrmions[16] are three-dimensional topological defects on a two-dimensional plane. They have been observed in solid materials[17–20] and in liquid crystals[21,22]. Skyrmions have recently been demonstrated in optics[23–26] and particularly in plasmonic systems[27,28] through the interference of surface plasmon polariton (SPP) waves. However, such non-trivial topologies have yet to be explored in optical moiré superlattices in general, and specifically in plasmonics.

Here we introduce 'plasmonic twistronics', which combines the tunability of moiré superlattices with the topology of skyrmion lattices to create optical fields with exotic topological features. With this method, we discovered structures displaying a unique topology, which we identified as skyrmion bags[19,22,29]. These bags are multi-skyrmion textures that consist of N skyrmions contained within a skyrmion boundary of opposite winding number. In addition, moiré superlattices generate supercells with a very large topological charge and can contain such a skyrmion bag at their centres. We demonstrate theoretically and experimentally that the twist angle between

[1]4th Physics Institute, Research Center SCoPE, and Integrated Quantum Science and Technology Center, University of Stuttgart, Stuttgart, Germany. [2]Faculty of Physics and Center for Nanointegration Duisburg-Essen (CENIDE), University of Duisburg-Essen, Duisburg, Germany. [3]Andrew and Erna Viterbi Department of Electrical Engineering, Technion – Israel Institute of Technology, Haifa, Israel. [4]School of Physics, University of Melbourne, Parkville, Victoria, Australia. e-mail: giessen@pi4.uni-stuttgart.de

https://doi.org/10.1038/s41567-025-02873-1

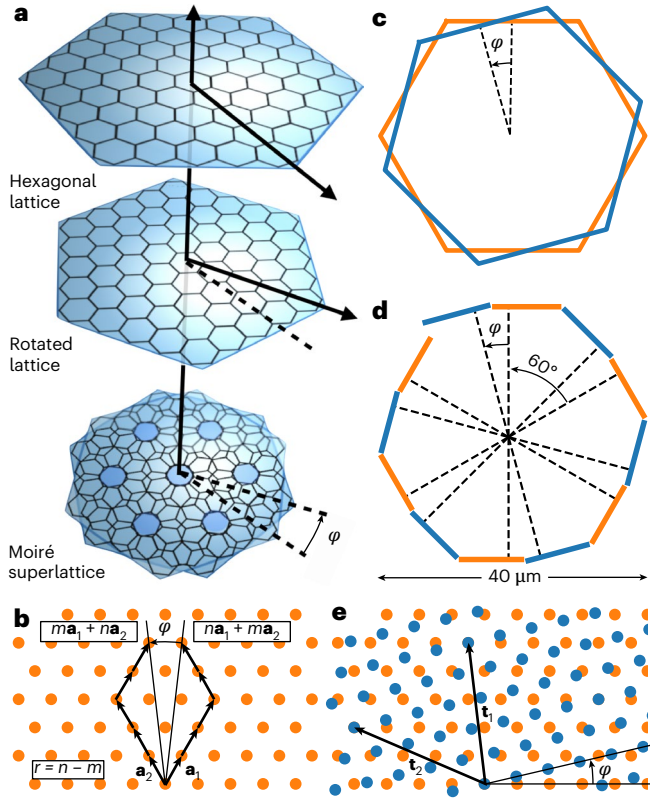

Fig. 1 | Hexagonal moiré lattices in solid state physics and plasmonics. **a**, Two superimposed lattices with a relative twist create a moiré superlattice with the same symmetry. **b**, Commensurate real-space lattices are created using twist angle φ that rotates an atom from position $n\mathbf{a}_1 + m\mathbf{a}_2$ to $m\mathbf{a}_1 + n\mathbf{a}_2$. The rotation is denoted by the integers m and $r = n - m$. **c**, A skyrmion lattice is created by exciting SPPs along a hexagonally shaped boundary. Two twisted hexagonally shaped boundaries result in a moiré skyrmion superlattice. **d**, Resulting schematic structure from which SPPs are emitted to create a moiré skyrmion lattice with twist angle φ. The boundaries are shifted inwards akin to an Archimedean spiral to counter the geometric phase arising from the circularly polarized pump pulse. **e**, Moiré superlattice and superlattice vectors $\mathbf{t}_1$ and $\mathbf{t}_2$ for the rotation φ indicated in **b**.

hexagonal skyrmion lattices controls the size of the skyrmion bags and their overall topological charge. We show the robustness of the skyrmion bags against twist-angle deviations. Our experiments reveal the full vectorial electric field distributions of the plasmonic system in both time and space, which confirm that the supercells of periodic (commensurate) moiré skyrmion lattices have characteristic higher-order topological charges. Our introduction of plasmonic twistronics offers a way to generate structured light fields with complex local topology and applications in super-resolution microscopy[30].

Plasmonic moiré superlattices

SPPs are electromagnetic surface waves confined to the interface between metals and dielectrics. They can be excited by laser pulses incident on edges, grooves or ridges in a metal surface to form interference patterns exhibiting different topological features in their electric field vectors[27,31] and their spin angular momentum vectors[28,32–34]. SPP waves excited from hexagonal boundaries create plasmonic skyrmion lattices, with a topology dependent upon the position of the boundaries and the resulting phase shift of the SPPs[27,35]. Plasmonic skyrmion lattices exhibit a sixfold symmetry[34], like the two-dimensional honeycomb lattices in graphene and hexagonal boron nitride. Moiré lattices have been studied intensively in these systems, especially in twisted bilayer graphene. They are created by twisting the lower layer of the material relative to the lattice of the upper layer by the moiré twist angle φ. Superimposing the two layers results in the moiré superlattice (Fig. 1a). Moiré superlattices have long-range aperiodic order and are, hence, quasicrystalline for general twist angles[36,37], thus enabling topological quasiperiodic lattices[38] with novel rotational point symmetries (two-, three-, four- and sixfold) and a variety of different combinations of topological textures. Nonetheless, for specific twist angles, periodic structures can be obtained by rotating one layer over another layer such that two lattice sites overlap. All commensurate structures in sixfold symmetry have been derived previously for graphene[1,39] and can be denoted by the integers m and n with the corresponding mapping

$$m\mathbf{a}_1 + n\mathbf{a}_2 \rightarrow n\mathbf{a}_1 + m\mathbf{a}_2, \qquad m, n \in \mathbb{Z}, \tag{1}$$

as illustrated in Fig. 1b.

We created moiré skyrmion superlattices by exciting SPP waves from a boundary resembling two twisted hexagons (Fig. 1c). Each hexagon contributed a skyrmion lattice. In practice, we can combine the two hexagons to create an excitation boundary consisting of 12 segments with the interleaved and twisted hexagonal structures shown in Fig. 1d in orange and blue. Neighbouring boundaries of the same colour have a relative angle of 60° for a hexagon, whereas the relative angle between neighbouring orange and blue line segments is the moiré twist angle φ. Circularly polarized light was used to excite the SPPs from every boundary, resulting in a spin to orbital angular momentum conversion and an unwanted phase shift[32,35]. This phase shift was compensated for by adjusting the positions (dashed lines in Fig. 1c) of the boundaries akin to an Archimedean spiral[40].

We generated with this technique a family of moiré skyrmion superlattices based on the moiré mapping equation (equation (1)). Superlattices with small periods appeared at twist angles 21.8° ($m = 1$ and $r = n - m = 1$), 13.2° ($m = 2$ and $r = 1$, as in Fig. 1e), 9.4° ($m = 3$ and $r = 1$) and 16.4° ($m = 3$ and $r = 2$). The resulting moiré skyrmion lattices calculated for these twist angles are shown in Fig. 2 together with the corresponding superlattice vectors $\mathbf{t}_1$ and $\mathbf{t}_2$, as well as the moiré periodicity. We derived the electric field distributions by assuming infinitely long boundary lines, which enabled the approximation of the SPP wave as a plane wave[41]. Damping of the plasmon wave was neglected (see Supplementary Note 4 for details). These approximations resulted in an infinitely large field of view, which allowed the periodicity to be clearly observed (top right images of Fig. 2a–d). The Fourier decomposition of the electric field (b_1 and b_2 in bottom right images of Fig. 2a–d) emphasizes the sixfold symmetry of the hexagonal excitation boundaries and the corresponding twist angles. Examining Fig. 2, it is clear that there is a cluster of skyrmions surrounded by a boundary at the centre of each supercell, a telltale sign hinting at the existence of skyrmion bags.

Although we focus in this work on moiré skyrmion superlattices formed in the SPP electric field, our findings can be readily extended to other forms of topological quasiparticles in wave systems[42,43]. In Supplementary Note 10, we present numerical results of moiré skyrmion and meron[44,45] superlattices with different rotation centres, as well as moiré spin skyrmion and spin meron superlattices (Supplementary Figs. 5–12). More specifically, we demonstrate that moiré meron lattices can harbour skyrmions and that, depending on the twist angle, the honeycomb spin meron lattice transforms into a hexagonal superlattice of spin merons, a honeycomb superlattice of spin skyrmions, or a hexagonal spin skyrmion lattice.

Topology of plasmonic skyrmion bags

The local topology of skyrmion vector fields can be characterized using the skyrmion number density:

$$s = \frac{1}{4\pi}\hat{\mathbf{e}} \cdot \left(\frac{\partial \hat{\mathbf{e}}}{\partial x} \times \frac{\partial \hat{\mathbf{e}}}{\partial y}\right), \tag{2}$$

https://doi.org/10.1038/s41567-025-02873-1

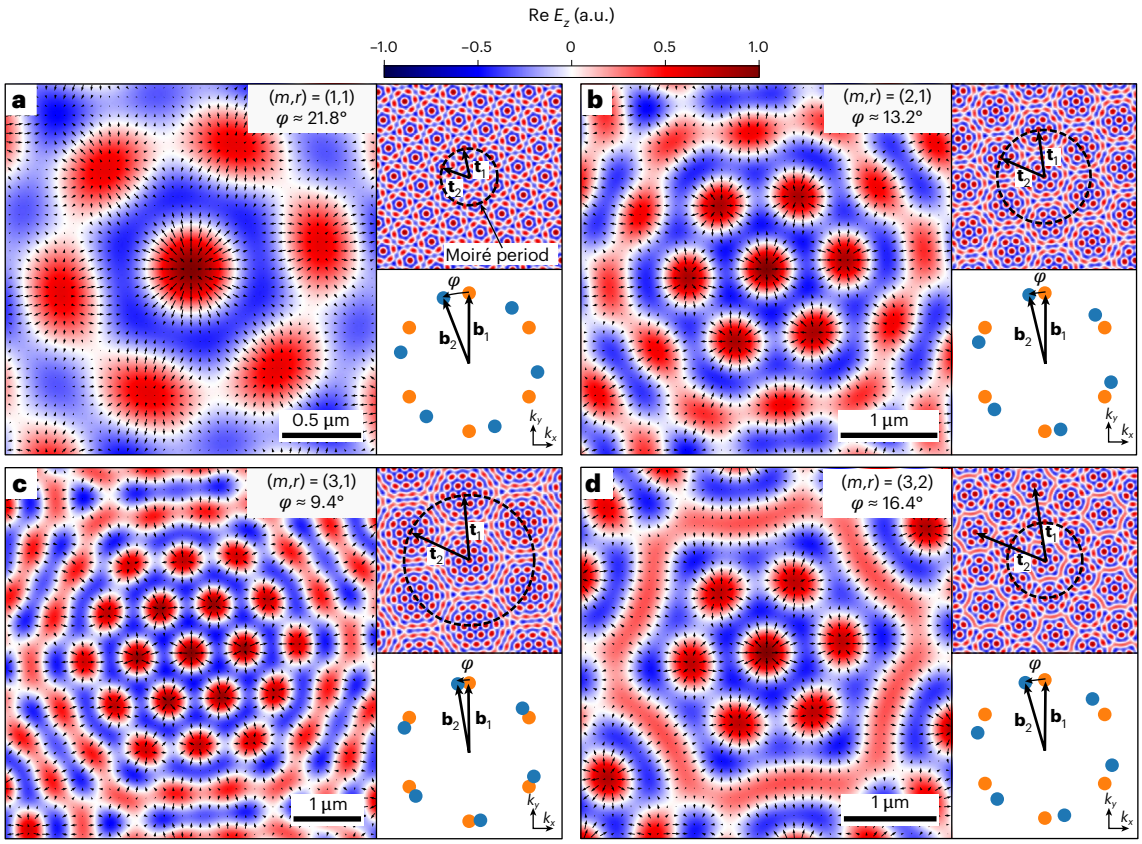

Fig. 2 | Simulated plasmonic moiré skyrmion lattices. a–d, Simulated electric field distributions of moiré skyrmion lattices with different commensurate twist angles φ: 21.8° (**a**), 13.2° (**b**), 9.4° (**c**) and 16.4° (**d**). Left, z component of the electric field as a colour plot and the in-plane components as a vector plot. Top right, zoomed-out view of size 20 × 20 µm^2 together with the moiré periodicity (indicted by a circle) and the superlattice vectors $\mathbf{t}_1$ and $\mathbf{t}_2$. Bottom right, schematic representation of the Fourier decomposition. The colours originate from the boundaries of Fig. 1c,d.

where $\hat{\mathbf{e}} = \mathbf{E}(\mathbf{r}, t)/|\mathbf{E}(\mathbf{r}, t)|$ is the unit vector of the SPP electric field. The skyrmion number or topological charge is defined by the surface integral $S = \int_\sigma s\, \mathrm{d}x\mathrm{d}y$, where σ is the local region that defines the quasiparticle. The skyrmion number counts the number of times the vectors wrap around the unit sphere. It can be further divided into two more topological numbers $S = p\nu$, where p is the polarity, defined by the direction of the out-of-plane vector components, and ν is the vorticity, which is determined by the direction of rotation in space of the in-plane field components[23,46].

Skyrmion bags, identified previously in liquid crystals[22] and chiral magnets[19,29], represent multi-skyrmion configurations, in which N skyrmions with $S = p = \nu = 1$ are enclosed within a larger skyrmion (Fig. 2). The surrounding skyrmion has the same vorticity but opposite polarity and, therefore, $S = -1$. Consequently, the total topological charge of a skyrmion bag is $S_{\mathrm{bag}} = (N - 1)$.

Moiré lattices give rise to the formation of skyrmion bags through the superposition of two skyrmion lattices in a single plane. The twist rotates the skyrmions of one lattice around a centre of rotation. When a skyrmion of the rotated lattice fills the gap between two skyrmions of the unrotated lattice, their interference creates an elongated region with a positive z component of the electric field. For suitable twist angles and centres of rotation, this region forms a closed loop and, hence, a bag skyrmion enclosing a set of N individual skyrmions (Fig. 2), thus forming the skyrmion bag.

When the lattice twist forms a periodic superlattice, the skyrmion bags become periodic in space and can be found in several super unit cells. However, the skyrmion bags are always smaller than the supercells, so that skyrmion bags cannot be used to tessellate the entire two-dimensional plane. Instead, the superlattice unit cell is rigorously defined and is associated with a well-defined topological invariant that can become very large, depending on the twist angle (Supplementary Table 1). Its robustness is somewhat unique, as higher-order real-space topological charges tend to be unstable[47].

Experimental observation of plasmonic skyrmion bags

We observed SPP skyrmion bags by measuring the spatio-temporal dynamics of the SPP electric field using time-resolved two-photon photoemission (2PPE) polarimetric photoemission electron microscopy (PEEM)[31,48,49], as illustrated in Fig. 3a. In this method, a laser pulse normally incident to the metal surface generated propagating SPP waves from grooves etched into a single-crystal gold flake using ion-beam milling (Fig. 3b). The pump pulse had a centre wavelength of 800 nm, which excited long-range SPPs with a wavelength $\lambda_{\mathrm{SPP}} = 780$ nm. The distribution of these waves was probed after a short time delay $\Delta\tau$ using several other laser pulses of different polarization[32,49]. The energy provided by the SPP wave and the probe pulse resulted in two-photon absorption and the emission of photoelectrons from the metal surface[50], which were imaged by PEEM. As the electron yield of this process was low, many repeated measurements were performed using a femtosecond laser with 80 MHz repetition rate to obtain sufficient image statistics of the electron emission. The time evolution of the propagation and interference of the SPP waves can be studied by repeating this process for a series of different pump–probe delays $\Delta\tau$. An exemplary electron emission from the experiment is presented in Fig. 3c.

After applying Fourier filters to the fundamental SPP momentum and frequency to isolate the relevant signal from the multitude of different contributions[49,50], we retrieved the in-plane components of the

https://doi.org/10.1038/s41567-025-02873-1

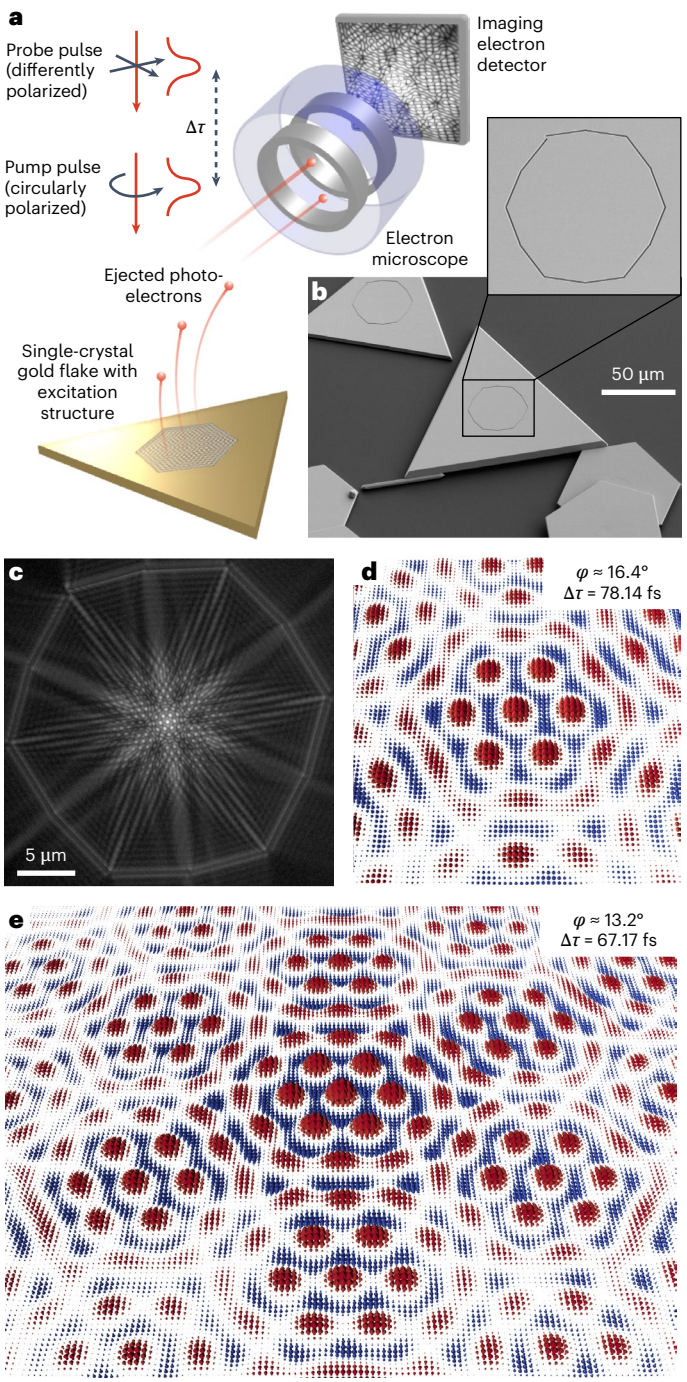

Fig. 3 | Ultrafast time-resolved vector microscopy of plasmonic skyrmion bags. a, 2PPE-PEEM measurement method. The femtosecond-laser pump–probe technique uses polarized beams combined with two-photon electron emission in an electron microscope to enable the retrieval of all vector components of the electric field of propagating SPPs as a function of time $\Delta\tau$. **b**, Scanning electron microscopy images of the 16.4° structure according to Fig. 1d. The grooves were milled into single-crystal gold flakes by ion-beam lithography. **c**, Fourier-filtered PEEM measurement of the plasmonic excitations. **d**,**e**, Reconstructed vector field components of SPP skyrmion bags at different twist angles φ, 16.4° (**d**) and 13.2° (**e**). Vectors with positive (negative) z component are drawn in red (blue).

electric field vectors above the surface. Subsequently, the out-of-plane component was calculated using Maxwell's equations. This method allowed us to reconstruct the SPP electric field components from the PEEM measurements (Fig. 3d,e) from which we can analyse the topology of the vector field.

Our experimental method yielded the temporal dynamics of the electric field vectors, which revealed a periodic transition from a skyrmion bag with a topological charge of $+(N-1)$ to a skyrmion bag with a topological charge of $-(N-1)$ and back within one optical cycle. Thereby, the signs of the topological charge of both the bag skyrmion and the skyrmions inside the bag changed analogous to the time dynamics observed in untwisted skyrmion lattices[31]. The period of this transition was determined by the excitation pump pulse, with the length of one optical cycle being 2.67 fs for a free-space wavelength of 800 nm (for results, see Extended Data Fig. 1). Animations of the time dynamics of a skyrmion bag are provided in the Supplementary Videos 1–4.

Using a structure with a twist angle of 16.4° (Fig. 3b–d), a skyrmion bag was observed for several frames in each optical cycle over an entire measurement sequence, taken with delay times $\Delta\tau$ between 57 and 96 fs. The reconstructed field vectors are shown in Fig. 3d for a delay time of $\Delta\tau = 78.14$ fs. The experimental results (Fig. 4d–f) are compared with numerical results (Fig. 4a–c) calculated using the method outlined in ref. 41, which simulates the entire 2PPE-PEEM measurement. These data show both the out-of-plane component of the electric field vector, represented by a colour plot, and the in-plane components in a vector plot. We observed notable agreement between experiment and theory. It is important to note that a feature can be classified as a skyrmion bag only if it satisfies the condition that the enclosed skyrmions have an individual topological charge opposite to that of the bag skyrmion. We examined this condition with our experimental data using the vorticity, the polarity and the local topological charges. The vorticity could be visually analysed along closed-loop lines along which the field only has an in-plane vector component. These lines appear coloured in Fig. 4b,e. As the out-of-plane fields along the boundary of the bag skyrmion are oppositely directed to those of the enclosed skyrmions (Fig. 4a,d), the polarity p of the bag skyrmion is opposite to that of the enclosed skyrmions. However, the azimuthal angle of the in-plane vector fields rotated in the same direction (Fig. 4b,e), so that both the bag and the enclosed skyrmions had the same vorticity $v = +1$. This led to the bag skyrmion having the opposite net skyrmion number density (Fig. 4c,f) compared to the enclosed skyrmions, which verifies that we had, indeed, created a skyrmion bag. As the SPP wavelength was close to the excitation wavelength, the amplitude of the in-plane field components was smaller than that of the out-of-plane field components. The Néel-type skyrmion vector texture, therefore, appeared bubble-like in the skyrmion number density. By integrating the skyrmion number density, the topological charge for the skyrmion bag $S_{bag} = 6$ whereas that for the skyrmions inside the bag $S_{cluster} = 7$. As with previous approaches[28,45], the integration boundary was the path along which the electric field had a maximum out-of-plane component. The numerical and experimental results fulfil the skyrmion bag requirements for a twist angle of 16.4°. Note that the accuracy of the skyrmion numbers depends on the resolution of the data used in the numerical integration. By using interpolation methods, the results converged to integer values (details in Supplementary Note 8).

The skyrmion bag appeared over a range of twist angles around an optimum angle, resulting in topological robustness against twist-angle rotations. The topological robustness of this structure with changes in twist angle were observed both in the simulations for a range of twist angles between 11.7° and 19.3° and in the experiments for the commensurate twist angle of 13.2° (for results, see Fig. 3d and Extended Data Figs. 2 and 3). In general, larger twist angles resulted in smaller skyrmion bags that were defined over a more extended range of twist angles and, therefore, had increased robustness against twist-angle rotations.

More complex skyrmion bags

Based on moiré theory, the moiré skyrmion lattice and, in turn, the skyrmion bags were limited to lattice structures with hexagonal symmetry. Thus, our method only permits skyrmion bags with specific numbers

https://doi.org/10.1038/s41567-025-02873-1

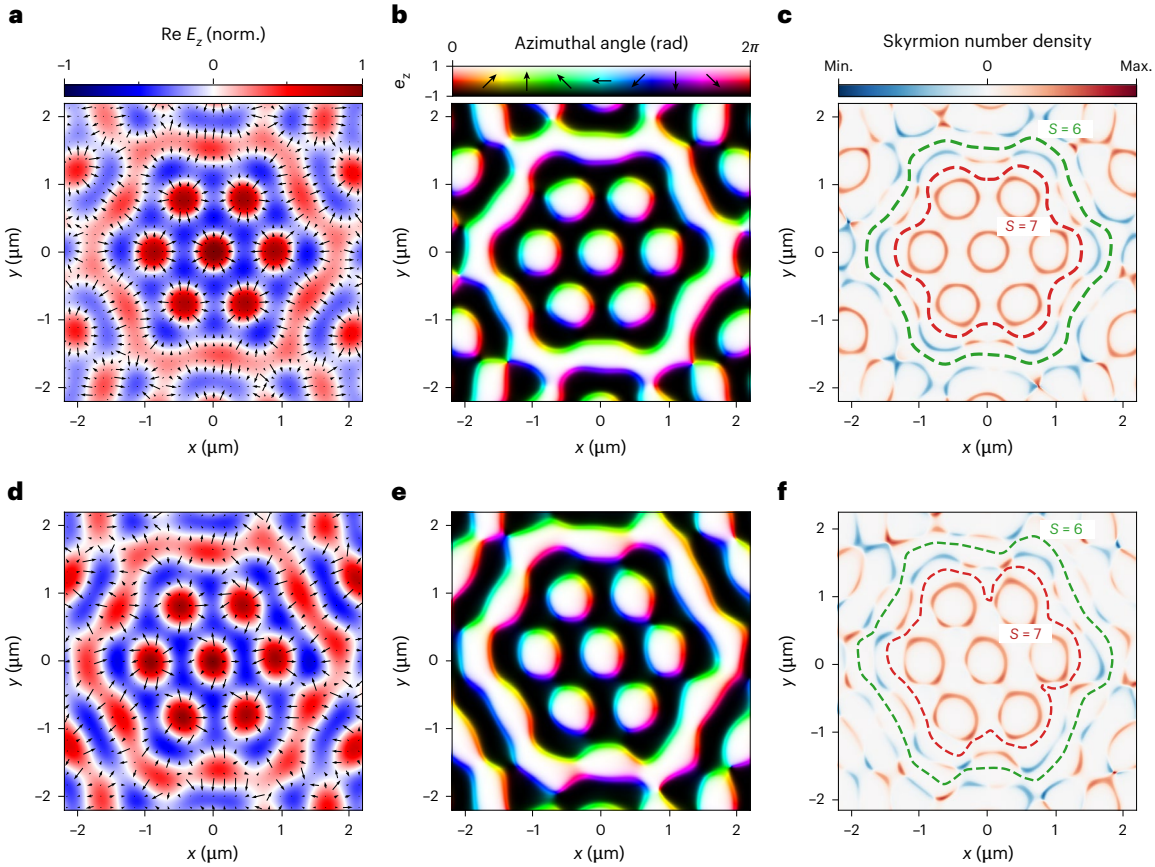

Fig. 4 | Analysis of PEEM simulation results and experimental results of a skyrmion bag with seven skyrmions. a,**d**, Electric field distribution for the ($m = 3, r = 2$) structure with a twist angle $\varphi = 16.43°$. **a**, Simulation results. **d**, Experimental results. The out-of-plane component is illustrated using the colour plot and the in-plane component of the electric field is depicted using the vector plot. The experimental results were obtained with a delay time $\Delta\tau = 78.14$ fs. **b**,**e**, Distributions of the out-of-plane amplitude (brightness) and in-plane orientation (colour) of the normalized electric field. **b**, Simulation results. **e**, Experimental results. Coloured areas indicate closed-loop lines, along which the electric field vectors only have an in-plane component. The in-plane orientation of the field vectors rotated by 2π along these lines for all skyrmions. **c**,**f**, Skyrmion number density of the electric field. **c**, Simulation results. **f**, Experimental results. Integration of the skyrmion number density yielded the total skyrmion number, which was calculated as $S_{bag} = 6$ for the total skyrmion bag (green dashed lines) and as $S_{cluster} = 7$ for the skyrmion cluster inside the bag (red dashed lines). Max., maximum; Min., minimum; norm., normalized.

of skyrmions within the bag. For example, if the centre of rotation is at a skyrmion lattice site, as is the case in Fig. 2, only skyrmion bags with 1, 7, 19, 37, … skyrmions in the bag can be created. Larger skyrmion bags appear for lower twist angles. For twist angles between 21.5° and 30°, a skyrmion bag with one skyrmion is formed, which is also referred to as a skyrmionium[23] (Extended Data Figs. 4 and 5; for details, see Supplementary Note 7).

So far, only twists around the skyrmion lattice site in the centre of the structure have been considered. However, the symmetry point of the twist plays an important role in the resulting topology. Skyrmion bags with different sizes were created by changing the centre of rotation to other symmetry points of the lattice, as shown in the PEEM simulations in Fig. 5. This includes the set of points P_2 in the middle of two neighbouring skyrmions at, for example, $\mathbf{a}_1/2$ and the set of points P_3 with equal distance to three surrounding skyrmions at, for example, $(2\mathbf{a}_1 - \mathbf{a}_2)/3$. With these extra rotation centres, we found other skyrmion bags of various sizes. The smallest ones were skyrmion bags with 2, 3, 4, 10, 12 or 14 skyrmions. Thus, by using the right twist angle and centre of rotation, it is possible to generate a tailored skyrmion bag with chosen total skyrmion number inside the moiré super cell.

Outlook

Plasmonic twistronics provides an avenue for creating electric field distributions with novel and robust topological configurations, with arbitrarily large topological invariants, a long-standing goal in the budding studies of topological light quasiparticles. We expanded our concept to meron lattices and topological textures in the spin angular momentum. Further generalizations to multi-layer moiré superlattices are possible by superimposing three or more lattices[51]. In essence, our methods and results can be used to create topological states in propagating light, as well as in various other wave systems[42,43].

In general, the ability to control the topological properties of light is important for novel light–matter interactions and could be useful for applications such as spin-optics, imaging, as well as topological and quantum technologies. This is particularly important in structured light microscopy[52], for super-resolution down to the single nanometre range[51] and for structured light–matter interactions, for example non-dipolar transitions with $\Delta l \neq 1$ (ref. 53) induced by light fields with non-zero local orbital angular momenta in Rydberg excitons in Cu_2O (ref. 54) or transition metal dichalcogenides[55]. Speculatively, it also opens up a pathway to encode information within the (controllable) topological charge of a skyrmion bag.

Online content

Any methods, additional references, Nature Portfolio reporting summaries, source data, extended data, supplementary information, acknowledgements, peer review information; details of author contributions and competing interests; and statements of data and code availability are available at https://doi.org/10.1038/s41567-025-02873-1.

https://doi.org/10.1038/s41567-025-02873-1

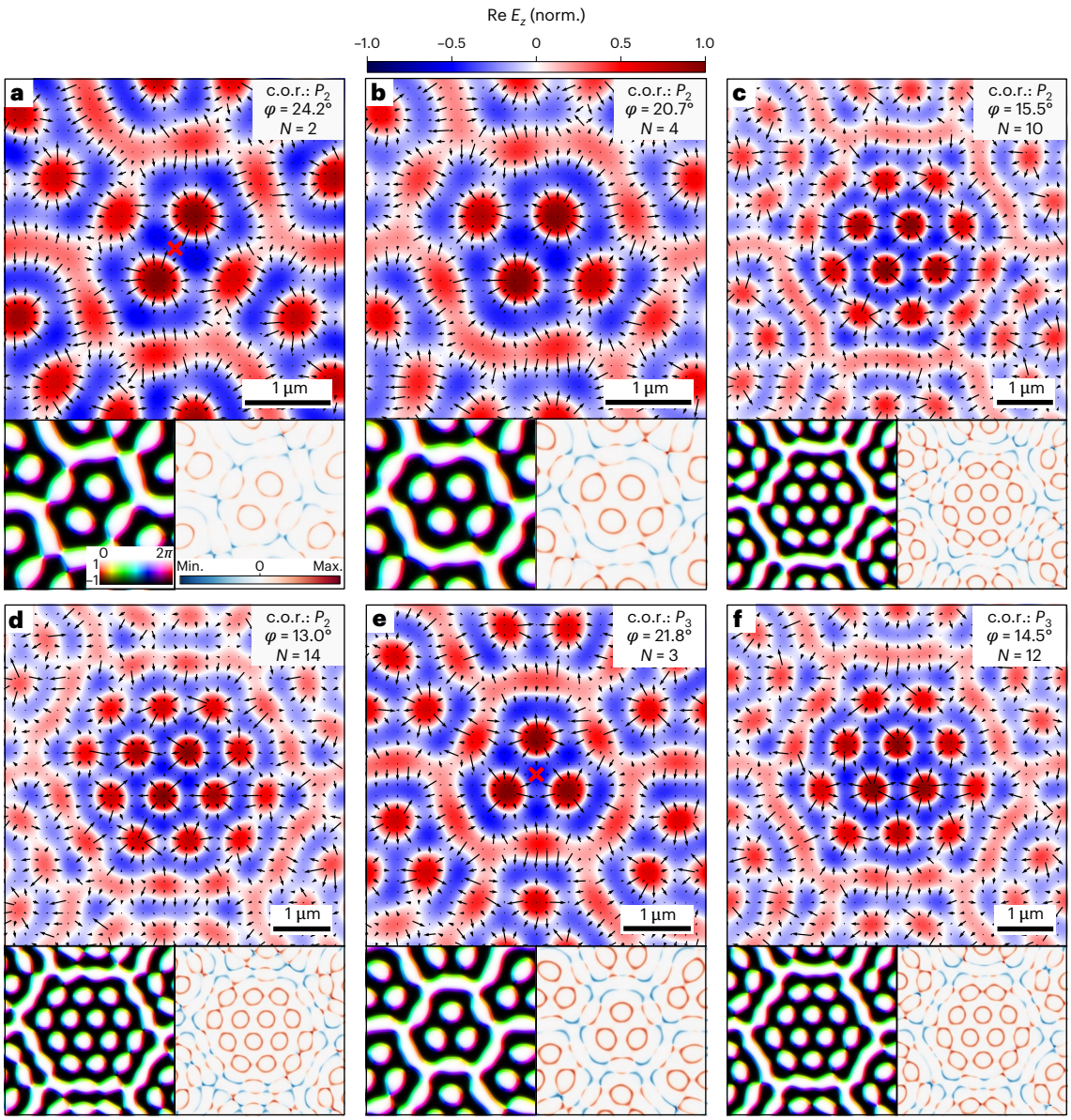

Fig. 5 | PEEM simulations of plasmonic skyrmion bags of different sizes. **a**–**f**, Skyrmion bags comprising 2 (**a**), 4 (**b**), 10 (**c**), 14 (**d**), 3 (**e**) or 12 (**f**) skyrmions. They were obtained using the twist angle φ and the centre of rotation P_2 at $\mathbf{a}_1/2$ (**a**–**d**) and P_3 at $(2\mathbf{a}_1 - \mathbf{a}_2)/3$ (**e**,**f**). The rotation centres are exemplarily marked by a red cross in **a** and **e**. The top images demonstrate the electric field distribution with the corresponding scale bar at the top of the figure. The out-of-plane component is illustrated using the colour plot, and the in-plane component of the electric field is depicted using the vector plot. Bottom left, distributions of out-of-plane amplitude (brightness) and in-plane orientation (colour) of the normalized electric field for the same area as the image at the top. Along the coloured lines, the electric field vectors only have an in-plane component. The in-plane orientation of the field vectors rotate by 2π along these closed-loop lines for all skyrmions. Bottom right, skyrmion number density of the electric field distribution in the top images. c.o.r., centre of rotation.

References

1. Campanera, J. M., Savini, G., Suarez-Martinez, I. & Heggie, M. I. Density functional calculations on the intricacies of moiré patterns on graphite. *Phys. Rev. B* **75**, 235449 (2007).
2. Shterman, D., Gjonaj, B. & Bartal, G. Experimental demonstration of multi moiré structured illumination microscopy. *ACS Photonics* **5**, 1898–1902 (2018).
3. Efremidis, N. K., Sears, S., Christodoulides, D. N., Fleischer, J. W. & Segev, M. Discrete solitons in photorefractive optically induced photonic lattices. *Phys. Rev. E* **66**, 046602 (2002).
4. Wang, P. et al. Localization and delocalization of light in photonic moiré lattices. *Nature* **577**, 42–46 (2019).
5. Fu, Q. et al. Optical soliton formation controlled by angle twisting in photonic moiré lattices. *Nat. Photonics* **14**, 663–668 (2020).
6. Wang, P. et al. Two-dimensional Thouless pumping of light in photonic moiré lattices. *Nat. Commun.* **13**, 6738 (2022).
7. Guan, J. et al. Far-field coupling between moiré photonic lattices. *Nat. Nanotechnol.* **18**, 514–520 (2023).
8. González-Tudela, A. & Cirac, J. I. Cold atoms in twisted-bilayer optical potentials. *Phys. Rev. A* **100**, 053604 (2019).
9. Luo, X. W. & Zhang, C. Spin-twisted optical lattices: tunable flat bands and Larkin-Ovchinnikov superfluids. *Phys. Rev. Lett.* **126**, 103201 (2021).
10. Cao, Y. et al. Unconventional superconductivity in magic-angle graphene superlattices. *Nature* **556**, 43–50 (2018).
11. Zheng, Z. et al. Unconventional ferroelectricity in moiré heterostructures. *Nature* **588**, 71–76 (2020).
12. Cao, Y. et al. Correlated insulator behaviour at half-filling in magic-angle graphene superlattices. *Nature* **556**, 80–84 (2018).

13. Park, H. et al. Observation of fractionally quantized anomalous Hall effect. *Nature* **622**, 74–79 (2023).
14. Chen, G. et al. Tunable correlated Chern insulator and ferromagnetism in a moiré superlattice. *Nature* **579**, 56–61 (2020).
15. Khalaf, E., Chatterjee, S., Bultinck, N., Zaletel, M. P. & Vishwanath, A. Charged skyrmions and topological origin of superconductivity in magic-angle graphene. *Sci. Adv.* **7**, eabf5299 (2021).
16. Skyrme, T. H. R. A unified field theory of mesons and baryons. *Nucl. Phys.* **31**, 556–569 (1962).
17. Yu, X. Z. et al. Real-space observation of a two-dimensional skyrmion crystal. *Nature* **465**, 901–904 (2010).
18. Mühlbauer, S. et al. Skyrmion lattice in a chiral magnet. *Science* **323**, 915–919 (2009).
19. Tang, J. et al. Magnetic skyrmion bundles and their current-driven dynamics. *Nat. Nanotechnol.* **16**, 1086–1091 (2021).
20. Das, S. et al. Observation of room-temperature polar skyrmions. *Nature* **568**, 368–372 (2019).
21. Fukuda, J. I. & Žumer, S. Quasi-two-dimensional skyrmion lattices in a chiral nematic liquid crystal. *Nat. Commun.* **2**, 246 (2011).
22. Foster, D. et al. Two-dimensional skyrmion bags in liquid crystals and ferromagnets. *Nat. Phys.* **15**, 655–659 (2019).
23. Shen, Y. et al. Optical skyrmions and other topological quasiparticles of light. *Nat. Photonics* **18**, 15–25 (2023).
24. Gao, S. et al. Paraxial skyrmionic beams. *Phys. Rev. A* **102**, 053513 (2020).
25. Shen, Y., Hou, Y., Papasimakis, N. & Zheludev, N. I. Supertoroidal light pulses as electromagnetic skyrmions propagating in free space. *Nat. Commun.* **12**, 5891 (2021).
26. Ornelas, P., Nape, I., de Mello Koch, R. & Forbes, A. Non-local skyrmions as topologically resilient quantum entangled states of light. *Nat. Photonics* **18**, 258–266 (2024).
27. Tsesses, S. et al. Optical skyrmion lattice in evanescent electromagnetic fields. *Science* **361**, 993–996 (2018).
28. Du, L., Yang, A., Zayats, A. V. & Yuan, X. Deep-subwavelength features of photonic skyrmions in a confined electromagnetic field with orbital angular momentum. *Nat. Phys.* **15**, 650–654 (2019).
29. Yang, L. et al. Embedded skyrmion bags in thin films of chiral magnets. *Adv. Mater.* **36**, 2403274 (2024).
30. Zheludev, N. I. & Yuan, G. Optical superoscillation technologies beyond the diffraction limit. *Nat. Rev. Phys.* **4**, 16–32 (2021).
31. Davis, T. J. et al. Ultrafast vector imaging of plasmonic skyrmion dynamics with deep subwavelength resolution. *Science* **368**, eaba6415 (2020).
32. Spektor, G. et al. Revealing the subfemtosecond dynamics of orbital angular momentum in nanoplasmonic vortices. *Science* **355**, 1187–1191 (2017).
33. Dai, Y. et al. Ultrafast microscopy of a twisted plasmonic spin skyrmion. *Appl. Phys. Rev.* **9**, 11420 (2022).
34. Lei, X. et al. Photonic spin lattices: symmetry constraints for skyrmion and meron topologies. *Phys. Rev. Lett.* **127**, 237403 (2021).
35. Tsesses, S., Cohen, K., Ostrovsky, E., Gjonaj, B. & Bartal, G. Spin-orbit interaction of light in plasmonic lattices. *Nano Lett.* **19**, 4010–4016 (2019).
36. Uri, A. et al. Superconductivity and strong interactions in a tunable moiré quasicrystal. *Nature* **620**, 762–767 (2023).
37. Lifshitz, R. Quasicrystals: a matter of definition. *Found. Phys.* **33**, 1703–1711 (2003).
38. Putley, H. J., Davies, B., Rodríguez-Fortuño, F. J., Bykov, A. Yu. & Zayats, A. V. Mixing skyrmions and merons in topological quasicrystals of evanescent optical field. Preprint at arxiv.org/abs/2409.03932 (2024).
39. Lopes dos Santos, J. M. B., Peres, N. M. R. & Neto, A. H. C. Continuum model of the twisted graphene bilayer. *Phys. Rev. B* **86**, 155449 (2012).
40. Gorodetski, Y., Niv, A., Kleiner, V. & Hasman, E. Observation of the spin-based plasmonic effect in nanoscale structures. *Phys. Rev. Lett.* **101**, 043903 (2008).
41. Davis, T. J. et al. Subfemtosecond and nanometer plasmon dynamics with photoelectron microscopy: theory and efficient simulations. *ACS Photonics* **4**, 2461–2469 (2017).
42. Ge, H. et al. Observation of acoustic skyrmions. *Phys. Rev. Lett.* **127**, 144502 (2021).
43. Smirnova, D. A., Nori, F. & Bliokh, K. Y. Water-wave vortices and skyrmions. *Phys. Rev. Lett.* **132**, 054003 (2024).
44. Ghosh, A. et al. A topological lattice of plasmonic merons. *Appl. Phys. Rev.* **8**, 41413 (2021).
45. Dai, Y. et al. Plasmonic topological quasiparticle on the nanometre and femtosecond scales. *Nature* **588**, 616–619 (2020).
46. Göbel, B., Mertig, I. & Tretiakov, O. A. Beyond skyrmions: review and perspectives of alternative magnetic quasiparticles. *Phys. Rep.* **895**, 1–28 (2021).
47. Berry, M. V. & Dennis, M. R. Knotted and linked phase singularities in monochromatic waves. *Proc. R. Soc. A: Math. Phys. Eng. Sci.* **457**, 2251–2263 (2001).
48. Kahl, P. et al. Direct observation of surface plasmon polariton propagation and interference by time-resolved imaging in normal-incidence two photon photoemission microscopy. *Plasmonics* **13**, 239–246 (2018).
49. Dreher, P. et al. Spatio-temporal topology of plasmonic spin meron pairs revealed by polarimetric photo-emission microscopy. *Adv. Photonics* **6**, 066007 (2024).
50. Dreher, P. et al. Momentum space separation of quantum path interferences between photons and surface plasmon polaritons in nonlinear photoemission microscopy. *Nanophotonics* **13**, 1593–1602 (2024).
51. Yang, A. et al. Spin-manipulated photonic skyrmion-pair for pico-metric displacement sensing. *Adv. Sci.* **10**, 2205249 (2023).
52. Shen, Y. et al. Roadmap on spatiotemporal light fields. *J. Opt.* **25**, 093001 (2023).
53. Neubauer, A. et al. Spectroscopy of nanoantenna-covered Cu_2O: towards enhancing quadrupole transitions in Rydberg excitons. *Phys. Rev. B* **106**, 165305 (2022).
54. Kazimierczuk, T., Fröhlich, D., Scheel, S., Stolz, H. & Bayer, M. Giant Rydberg excitons in the copper oxide Cu_2O. *Nature* **514**, 343–347 (2014).
55. Hill, H. M. et al. Observation of excitonic Rydberg states in monolayer MoS_2 and WS_2 by photoluminescence excitation spectroscopy. *Nano Lett.* **15**, 2992–2997 (2015).
56. Schwab, J. et al. Skyrmion bags of light in plasmonic moiré superlattices. *figshare* https://doi.org/10.6084/m9.figshare.28541801 (2025).

Data availability

The data supporting the findings of this study are available from the corresponding author upon reasonable request. Reconstructed electric field distributions of the PEEM measurements and PEEM simulations are available via Figshare at https://doi.org/10.6084/m9.figshare.28541801 (ref. 56). Source data are provided with this paper.

Code availability

The code used to produce the results are available from the corresponding author upon reasonable request.

Acknowledgements

We acknowledge support from the ERC (Complexplas, 3DPrintedoptics) (J.S., F.M., A.M., B.F. and H.G.), DFG (grant no. SPP1391 Ultrafast Nanooptics (J.S., F.M., A.M., B.F., H.G., A.N., P.D. and F.-J.M.z.H.), CRC 1242 Non-Equilibrium Dynamics of Condensed Matter in the Time Domain (project no. 278162697-SFB 1242 to A.N., P.D. and F.-J.M.z.H.), BMBF (Printoptics) (J.S., F.M., A.M., B.F. and H.G.), BW Stiftung (Spitzenforschung, Opterial) (J.S., F.M., A.M., B.F. and H.G.) and Carl-Zeiss Stiftung (J.S., F.M., A.M., B.F. and H.G.). T.J.D. acknowledges support from the MPI Guest Professorship Program and from the DFG (grant no. GRK2642) through a Photonic Quantum Engineers for a Mercator Fellowship. S.T. acknowledges support from the Adams fellowship programme of the Israel Academy of Science and Humanities, the Rothschild fellowship of the Yad Hanadiv Foundation, the VATAT-Quantum fellowship of the Israel Council for Higher Education, the Helen Diller Quantum Center postdoctoral fellowship and the Viterbi fellowship of the Technion – Israel Institute of Technology.

Author contributions

G.B and S.T. conceived the idea of twisted skyrmion lattices and skyrmion bags. J.S., F.M. and H.G. conceived the idea of the commensurate angles. J.S. and T.J.D. carried out the simulations, analytical calculations and skyrmion number analysis. A.N., P.D. and F.-J.M.z.H. carried out the PEEM experiment and vectorial retrieval. B.F., A.M. and H.G. grew the single-crystal gold flakes and carried out the ion-beam structuring. K.C., S.T. and G.B carried out the scanning near-field optical microscopy experiment. J.S., T.J.D., S.T., B.F. and H.G. wrote the paper. All authors contributed to the discussions and the final editing.

Competing interests

The authors declare no competing interests.

Additional information

Extended data is available for this paper at https://doi.org/10.1038/s41567-025-02873-1.

Supplementary information The online version contains supplementary material available at https://doi.org/10.1038/s41567-025-02873-1.

Correspondence and requests for materials should be addressed to Harald Giessen.

Peer review information *Nature Physics* thanks Henry Putley and the other, anonymous, reviewer(s) for their contribution to the peer review of this work.

https://doi.org/10.1038/s41567-025-02873-1

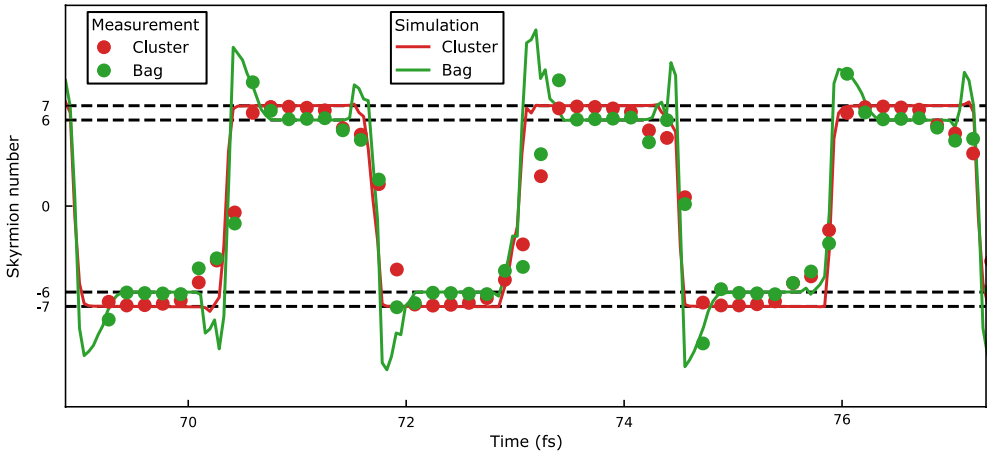

Extended Data Fig. 1 | Temporal analysis of PEEM measurement results. The experimental skyrmion number of the skyrmion bag and the cluster within in the bag are displayed as a function of the time delay between the pump and probe pulse in the PEEM experiment. The data is plotted together with the results obtained from the PEEM simulation (solid lines).

https://doi.org/10.1038/s41567-025-02873-1

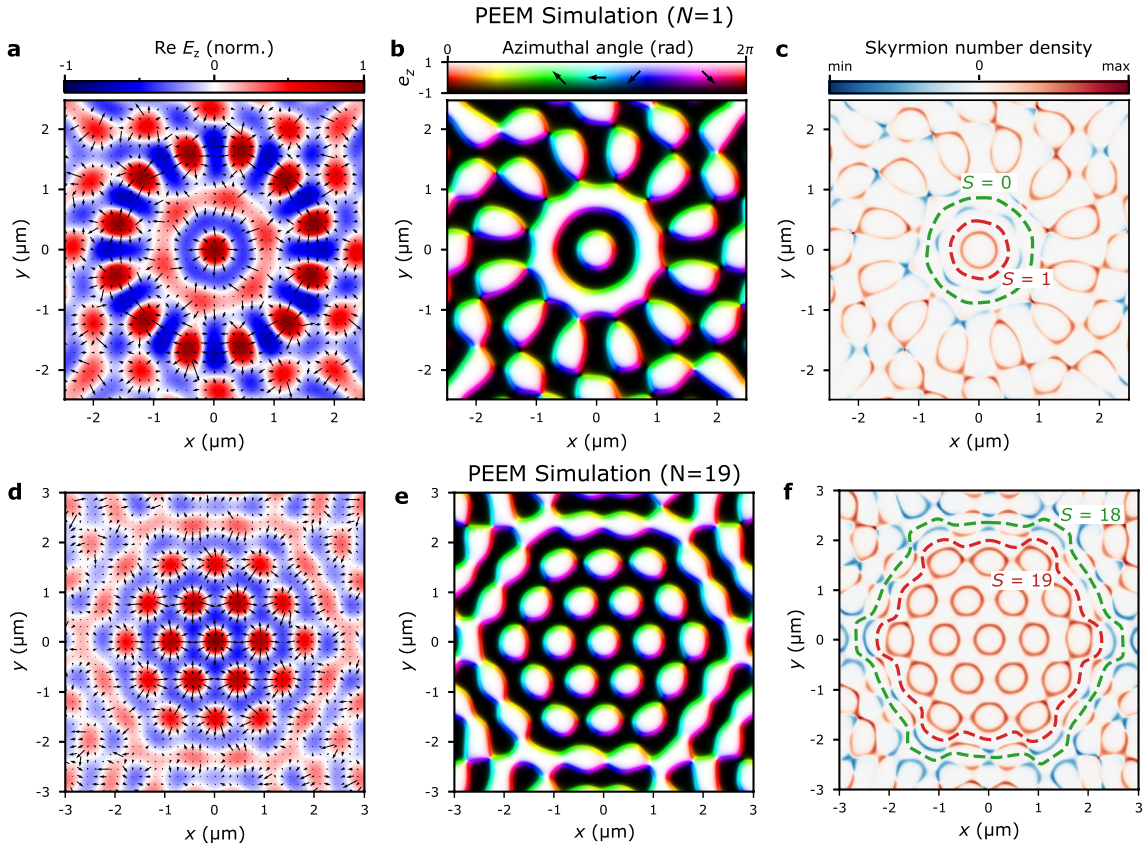

Extended Data Fig. 2 | Analysis of PEEM simulation results of a skyrmion bag comprising (a-c) *N*=1 skyrmion (skyrmionium) and (d-f) *N*=19 skyrmions. **a**, **d**, Electric field distribution exemplary for structures with twist angle φ=30° ($N = 1$) and φ=9.4° ($N = 19$). The out-of-plane component is illustrated using the color plot and the in-plane component of the electric field is depicted using the vector plot. **b**, **e**, Distributions of the out-of-plane amplitude (brightness) and in-plane orientation (color) of the normalized electric field. Colorful areas indicate closed-loop lines, along which the electric field vectors only have an in-plane component. The in-plane orientation of the field vectors rotates by 2π along these lines of all skyrmions. **c**, **f**, Skyrmion number density of the electric field. Integration of the skyrmion number density yields the total skyrmion number. For the total bag the integrated area is given by the enclosed space inside the dashed green line. The skyrmion cluster only counts the skyrmions inside the bag which means that in this case the skyrmion number density is integrated within the area surrounded by the dashed red line.

https://doi.org/10.1038/s41567-025-02873-1

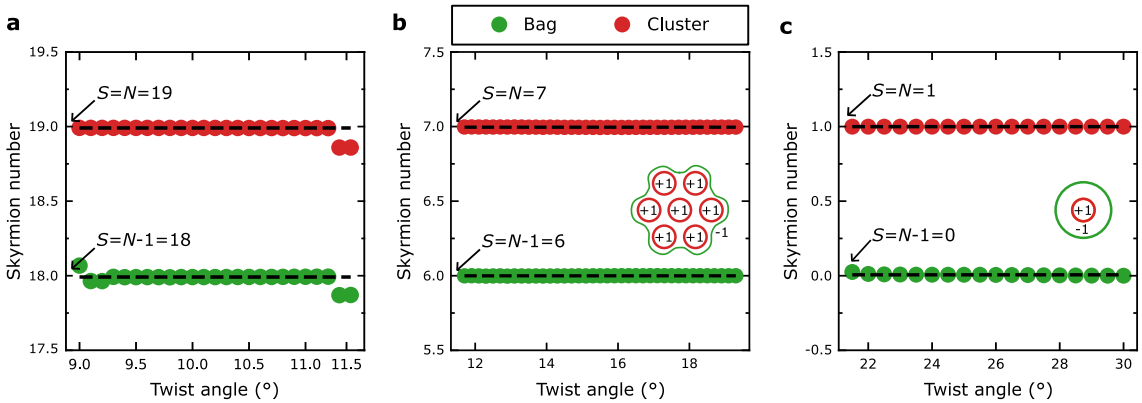

Extended Data Fig. 3 | Skyrmion number of the skyrmion bag and the skyrmion cluster inside the bag as a function of the twist angle for the skyrmion bags with 19 (a), 7 (b) and 1 (c) skyrmions in the bag. The skyrmion numbers are calculated by integrating the skyrmion number density. For the total bag, the integrated area is given by the enclosed space inside the green dashed line of Fig. 4c, f. The skyrmion cluster only counts the skyrmions inside the bag which means that the skyrmion number density is integrated within the area surrounded by the orange line of Fig. 4c, f. For the three different skyrmion bags, both skyrmion numbers remain constant over a wide range of twist angles.

https://doi.org/10.1038/s41567-025-02873-1

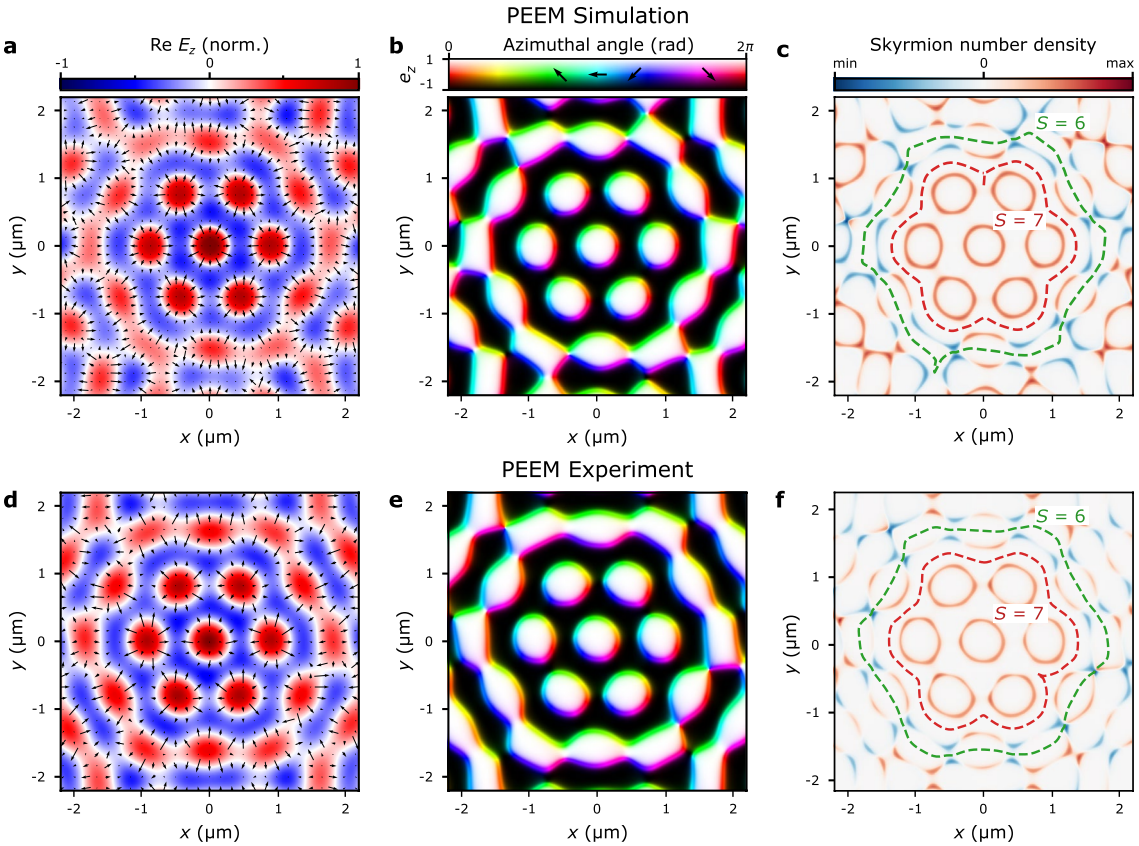

Extended Data Fig. 4 | Analysis of (a-c) PEEM simulation, (d-f) PEEM measurement results of a skyrmion bag with 7 skyrmions at twist angle of 13.2°. a, **d**, Electric field distribution. The out-of-plane component is illustrated using the color plot and the in-plane component of the electric field is depicted using the vector plot. **b**, **e**, Distributions of the out-of-plane amplitude (brightness) and in-plane orientation (color) of the normalized electric field. Colorful areas indicate closed-loop lines, along which the electric field vectors only have an in-plane component. The in-plane orientation of the field vectors rotates by 2π along these lines of all skyrmions. **c**, **f**, Skyrmion number density of the electric field. Integration of the skyrmion number density yields the total skyrmion number. For the total bag the integrated area is given by the enclosed space inside the green dashed line. The skyrmion cluster only counts the skyrmions inside the bag which means that the skyrmion number density is integrated within the area surrounded by the dashed red line.

https://doi.org/10.1038/s41567-025-02873-1

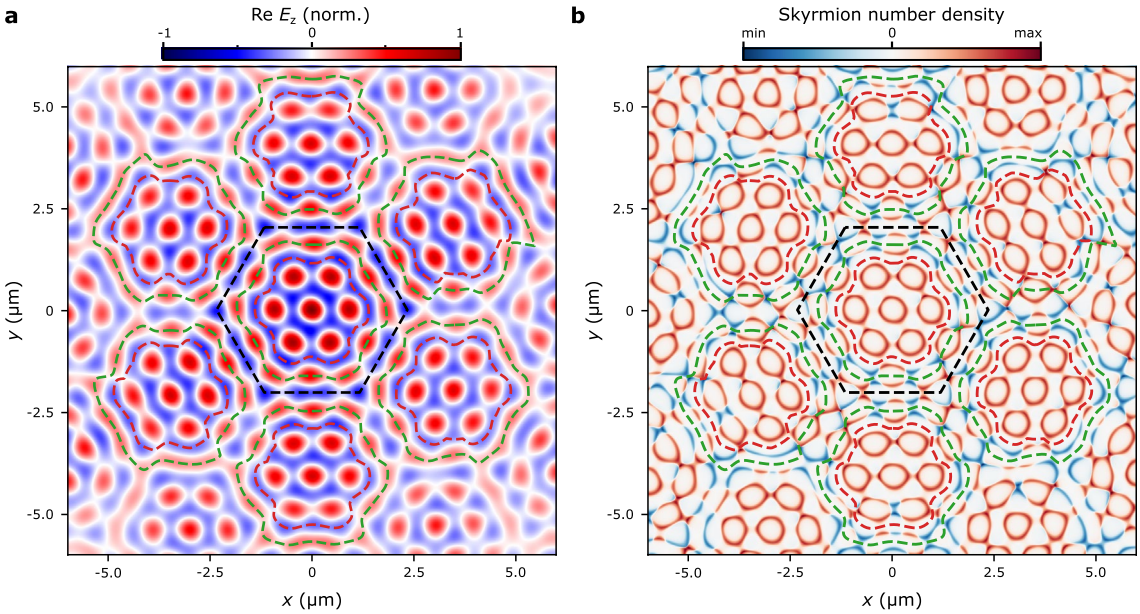

Extended Data Fig. 5 | Further analysis of PEEM measurement results of skyrmion bags with 7 skyrmions in a commensurate superlattice at 13.2° twist angle. a, Electric field distribution. The out-of-plane component is illustrated using the color plot. **b**, Skyrmion number density of the electric field. Integration of the skyrmion number density yields the total skyrmion number. For the total bags the integrated area is given by the enclosed space inside the green dashed lines. The skyrmion cluster only counts the skyrmions inside the bag, which means that the skyrmion number density is integrated within the area surrounded by the dashed red lines. In this measurement, three out of seven skyrmion bags of the observed superlattice have the correct skyrmion numbers of $S_{\mathrm{bag}} = 6$ and $S_{\mathrm{cluster}} = 7$. The center super-cell is surrounded by black dashed lines.